Two-Color High Harmonic Generation from Relativistic Plasma Mirrors

N. F. Beier* and F. Dollar
STROBE, NSF Science & Technology Center, University of California, Irvine, CA 92617 USA
(*nbeier@ualberta.ca)
(Dated: June 1, 2023)

High intensity, laser solid interactions are capable of generating attosecond light bursts via high harmonic generation, most work focuses on single beam interactions. In this study, we perform a numerical investigation on the role of wavelength and polarization in relativistic, high harmonic generation from normal-incidence, two-beam interactions off plasma mirrors. We find that the two-beam harmonic generation mechanism is a robust process described by a set of well-defined selection rules. We demonstrate that the emitted harmonics from normal incidence interactions exhibit an intensity optimization when the incident fields are of equal intensity for two-color circularly-polarized fields.

I. INTRODUCTION

Relativistic high order harmonic generation (HHG) driven by the reflection of light off an overdense plasma mirror offers a promising means of producing high-brightness, attosecond-duration light in the extreme ultraviolet (EUV) and soft x-ray regions that has been shown to extend to hundreds of harmonic orders[1–4]. Several mechanisms have been theoretically proposed and experimentally identified for the HHG mechanism including the relativistic oscillating mirror (ROM) model [5–8], coherent synchrotron emission (CSE) [9–11], and relativistic electronic spring (RES) model [12, 13].

As described in the ROM model, when an intense laser is incident on a plasma surface, the electrons that are driven into the plasma by the laser field experience a restoring force from the nearly-immobile ions. The electron motion becomes relativistic when the laser normalized field strength $a_0 = eE_0/m_e c\omega_0 \gtrsim 1$, where E_0 is the laser electric field, ω_0 the laser frequency, m_e the rest mass of electron, and e the fundamental electric charge. This leads to an oscillation of relativistic electrons near the relativistic critical surface, $n_e = \gamma n_c$ where γ is the relativistic factor of electrons and $n_c = m_e\varepsilon_0\omega_0^2/e^2$ is the non-relativistic critical density. The reflected laser field experiences a nonlinear phase shift due to the oscillating critical surface electrons, capable of producing higher energy photons. For multi-cycle lasers, this phase shift becomes periodic and leads to the generation of harmonics of the fundamental laser frequency. As the radiation is being emitted from one moving plasma surface, the process is inherently phase-matched enabling high single-shot flux.

The harmonics produced by the ROM mechanism have characteristic properties determined by the input laser and plasma parameters [1]. For example, the allowed harmonic orders and their individual polarization states are determined by the interaction geometry and critical surface oscillation modes[6]. A laser field reflecting off a surface at normal incidence produces a single mirror oscillation mode at frequency 2ω. The reflected field will contain the odd harmonics of the laser $\omega_n = (2n+1)\omega$. At oblique incidence, the symmetry of the interaction is broken and the surface can now oscillate at frequency ω. The reflected field will contain even harmonics polarized along the electric field direction, and odd harmonics polarized parallel or orthogonal to the electric field for p- and s-polarized interactions, respectively.

Recently, there has been increased interest in investigating the relativistic harmonic generation process through multi-beam interactions with a primary focus on two-color collinear studies. The introduction of the second harmonic to the driving field has been shown to provide benefits to relativistic HHG including the enhancement of harmonic conversion efficiency and attosecond burst isolation[14–18]. The choice of $\omega + 2\omega$ collinear studies is one of practical convenience due to the high conversion efficiencies of second harmonic generation crystals available for experiments. While most relativistic HHG studies have focused on the interaction of two linearly-polarized (LP) fields, there has also been increased interest in efficiently generating circularly-polarized (CP) harmonics. A scheme involving the interaction of elliptically-polarized light at an oblique incidence has been shown to produce circularly-polarized harmonics [19]. Furthermore, theoretical and computational work [20, 21] has shown that high-brightness, circularly-polarized harmonics can be generated in an analogous manner to circularly-polarized harmonics generated in the tunnel ionization regime from counter-rotating, circular fields in collinear [22, 23] and non-collinear [24] geometries even though it is a physically distinct regime.

Studies on two-beams interactions with plasma mirrors have up to this point been separated into either linear or circular polarization driven by $\omega + 2\omega$ fields. However, new multiwavelength laser facilities are coming online that use new laser technologies which allow arbitrary frequency combinations[25, 26]. The capability to combine multiple, non-commensurate frequencies, i.e. fields with frequency ratio $\omega_2/\omega_1 \neq \mathbb{Z}$, where ω_2 and ω_1 are the central frequencies of the fundamental fields, in a single interaction has not been examined extensively in the field to date, and a multi-beam framework for arbitrary frequencies does not currently exist.

In this Article, we show through the use of normal-incidence, particle-in-cell simulations that a set of two-color selection rules can be derived using the ROM model of relativistic harmonic generation, enabling control over the emission and polarization of the harmonics. Using non-commensurate frequencies enables a robust examination of

* Present address: Department of Electrical and Computer Engineering, University of Alberta, Edmonton, AB T6G 2R3 Canada

the laser-plasma coupling that results in unique and controllable harmonic spectra. We show that the harmonic properties and intensity optimization are governed by the relativistic critical surface oscillations during the laser reflection. The generated two-color harmonic spectra and polarization states are determined by the frequency ratio and polarization states of the fundamental fields, respectively. Additionally, we show that the intensity optimization of the two-color circularly-polarized harmonic generation process occurs at equal intensities of the fundamental fields, independent of frequency ratio.

II. METHODS

Numerical simulations were performed using the fully-relativistic, particle-in-cell code OSIRIS 4.0 [27]. For these two-color simulations, the physical quantities were normalized to the central wavelength, λ_1, and period, T_1, of the lower frequency laser. A series of 1D3V simulations were performed in a simulation region that was $X = 127\ \lambda_1$ units long with 128 particles per cell, using a grid size of 40,000 points. This results in a spatial resolution of $\Delta x = 3.2 \times 10^{-3}\ \lambda_1$. The simulations were run for a total time of $T = 47.7\ T_1$ with a time step of $\Delta t = 3.98 \times 10^{-3}\ T_1$. The plasma was initialized with bulk density $n_e = 100 n_{c,1}$ and thickness $7.96\ \lambda_1$. An exponential density ramp of the form $n_e = 100 n_c \exp(-x/L_s)$ was placed before the front surface of the target to represent pre-plasma formed by a laser pre-pulse before the high intensity interaction [28], where $L_s = \lambda_1/2\pi$ was used for the presented simulations, which is comparable to optimal scale-lengths from previous one-beam experimental studies [29–31]. Because we are investigating the short-pulse regime of laser-plasma interactions, which requires suitably short plasma-scale lengths, we consider the ions to act as an immobile background.

Two laser fields were initialized, each with a flat-top temporal profile of $\tau = 9\ T_1$. Flat-top temporal profiles were used to simplify the plasma dynamics, but comparisons between lasers with flat-top and Gaussian temporal profiles were performed to ensure the simulations gave consistent results regardless of pulse profile (see Supplemental Figure 7). The choice to use a relatively long pulse length of nine optical cycles was to easily discriminate between the individual harmonic orders produced during the interaction (see Supplemental Figure 8). The laser fields were initialized with two fundamental frequencies ω_1 and ω_2, normalized vector potentials $a_{0,1} = eE_1/m_e c\omega_1$ and $a_{0,2} = eE_2/m_e c\omega_1$, and either linear or circular polarization. Note, the second field does not have an independent normalization.

After the interaction the light reflected back into free space ($x < 0$). The electric field was then filtered to remove field contributions due to the bulk plasma target, i.e. for $E = 0$ for $x \geq 19.8\lambda_1$ while the laser pulse is entirely in the region $x < 19.8\lambda_1$. The electric field was then analyzed using fast Fourier-transforms (FFT). A small fraction of hot electrons in the vacuum are not filtered out since they overlap with the laser field, which will introduce a negligible amount of DC noise in the FFT. During the reflection, the relativistic critical surface, $\gamma n_c(x,t)$, was also tracked by taking into account the local Lorentz factor of the plasma electrons every ten simulation time steps. The resulting motion was then Fourier-transformed to extract the oscillation frequencies of the plasma.

Unless otherwise specified, the presented frequency ratio was $\omega_2/\omega_1 = 1.65$ and the total normalized vector potential was held constant at $a_0 = 10$. The choice of the presented frequency ratio is from considerations of frequency ratios produced by Ti:Sapphire-driven optical parametric amplification (OPA) sources, and eliminates the redundancy of certain beat frequencies produced by commensurate two-color fields. For a total vector potential of $a_0 = 10$ and central frequencies of $\omega_1 = 1$ and $\omega_2 = 1.65$, the individual normalized vector potential values were $a_{0,1} = 6.2$ and $a_{0,2} = 3.8$.

III. RESULTS

A. Linearly-Polarized Two-Color HHG

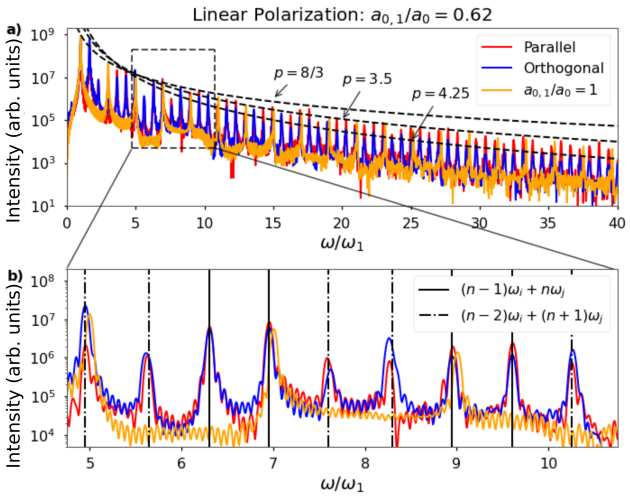

FIG. 1. Harmonic spectra of two-color, linearly-polarized (LP) fields. 1 a) Reflected spectrum of LP pulses at normal incidence. The parallel (red) and orthogonal (blue) fields contain additional harmonic orders beyond the odd harmonic orders expected from a single frequency interaction (yellow). 1 b) Zoom in between $\omega/\omega_1 = 5$ and $\omega/\omega_1 = 11$ with different harmonics denoted by vertical lines.

The reflected spectra of two LP laser fields with frequencies $\omega_1 = 1.0$ and $\omega_2 = 1.65$ can be seen in Fig 1 a). The polarization angle of the higher frequency field is rotated between 0^o and 90^o such that the field polarizations are parallel (red) and orthogonal (blue). As a reference, the reflected spectrum of a single color laser with central frequency ω_1 is plotted in yellow. Because the peak field strength of the orthogonal fields is reduced, the normalized vector potentials of the individual fields were increased by a factor of 1.37 in order to produce the same peak field strength of the pulse envelope as the parallel polarization case. To account for the difference in

total energy between the two interactions, the reflected spectra are normalized to the initial energy of the laser fields. Both parallel and orthogonal cases contain multiple harmonic channels that are separate from the odd harmonics produced from a single frequency at either ω_1 or ω_2. Four such channels, $(n-1)\omega_i + n\omega_j$ and $(n-2)\omega_i + (n+1)\omega_j$, where $i, j = 1, 2$ are plotted as vertical lines in Figure 1b. In general, the observed two-color HHG harmonics are

$$\Omega = n_1\omega_1 + n_2\omega_2, \tag{1}$$

where $n_1 + n_2 = 2k - 1$, and n_1, n_2, and $k \in \mathbb{Z}$.

The harmonic emission of the two-color fields follows a power-law decay of the form $I(n) \propto n^{-p}$, which is a well-known scaling for single-color relativistic high harmonic generation [4]. From previous single-color experiments, the decay constant has ranged between $5 < p < 10$ [30–33], with the theoretical ultra-relativistic limit, i.e. $a_0 \gg 1$, of the decay from the ROM model given by $p = 8/3$ [34]. Other models such as CSE have predicted decay constants less than $p = 8/3$ and can approach $p = 4/3$ in the ultra-relativistic limit [35]. The single-color and two-color with parallel polarization have comparable decay constants of $p = 3.5$, while the orthogonal polarization case has a stronger power law decay with $p = 4.25$.

B. Circularly-Polarized Two-Color HHG

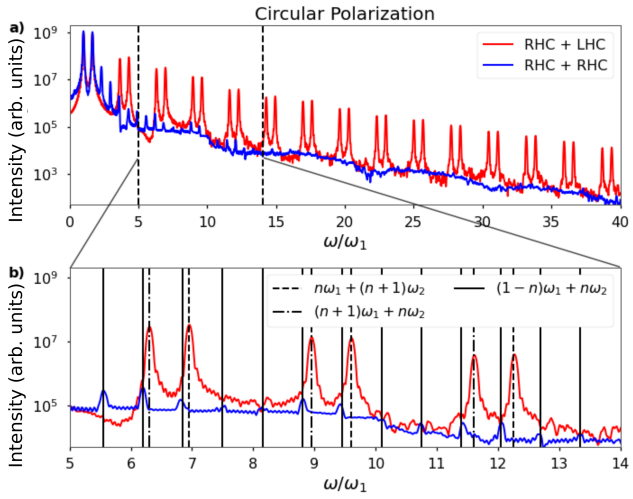

FIG. 2. Harmonic spectra of two-color, circularly-polarized (CP) fields. 2 a) Reflected spectrum of CP pulses at normal incidence. The two-color counter-rotating (red) and co-rotating (blue) fields. 2 b) Zoom in between $\omega/\omega_1 = 5$ and $\omega/\omega_1 = 14$ with different harmonic channels denoted by vertical lines.

The reflected spectra of two CP laser fields with frequencies ω_1 and ω_2 can be seen in Fig 2a. The polarization of the second field at frequency ω_2 is rotated such that the fields are counter-rotating (red) and co-rotating (blue). Observation of harmonics generated from two-color, CP fields is remarkably different from the single-color circular case, which does not produce harmonic emission from a normal incidence reflection. Two harmonic channels in the form of doublets are present in the counter-rotating case:

$$\Omega_+ = n\omega_2 + (n-1)\omega_1 \tag{2}$$

$$\Omega_- = (n-1)\omega_2 + n\omega_1. \tag{3}$$

Harmonics are also observed when the two fields are co-rotating, which is in agreement with recent results by Q. Li, et al [36]. These harmonics are circularly polarized and co-rotating with the incident fields with selection rules:

$$\Omega = n\omega_2 - (n-1)\omega_1 \tag{4}$$

For a constant peak normalized vector potential of $a_0 = 10$, the co-rotating harmonics have a much faster decay when compared to either the counter-rotating fields or linearly-polarized fields.

C. Variation of Frequency Ratio

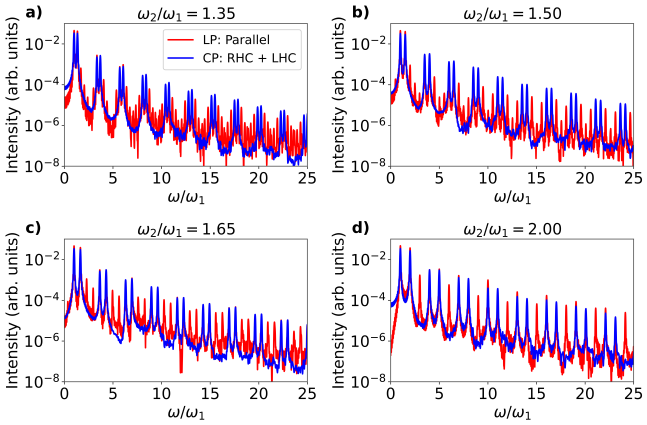

FIG. 3. Harmonic spectra of two-color LP (red) and CP (blue) fields for different frequency ratios of 3 a) $\omega_2/\omega_1 = 1.35$, 3 b) $\omega_2/\omega_1 = 1.5$, 3 c) $\omega_2/\omega_1 = 1.65$, and 3 d) $\omega_2/\omega_1 = 2$. The a_0 ratio for all cases were varied such that the field intensities were equal.

A direct comparison of the harmonics generated from different frequency ratios is shown in Figure 3. Harmonic spectra of two-color LP (red) and CP (blue) fields for different frequency ratios of 3 a) $\omega_2/\omega_1 = 1.35$, 3 b) $\omega_2/\omega_1 = 1.5$, 3 c) $\omega_2/\omega_1 = 1.65$, and 3 d) $\omega_2/\omega_1 = 2$. The a_0 ratio for all cases were varied such that the field intensities were equal, and the spectra have been normalized by the total energy of the incident fields. The number of observed harmonic channels for the LP case increases as the frequency ratio of the two fields approaches unity. For the $\omega_2/\omega_1 = 2$ case the observed LP harmonics constitute the even and odd order harmonics of ω_1. Conversely, the CP harmonics produced by counter-rotating fields are always observed as harmonic doublets, regardless of frequency ratio. For the a_0 ratio used the peak doublets for

the CP fields correspond to the locally-brightest harmonics in the LP case, and their comparable intensity implies that the CP harmonics are generated with similar efficiency as the LP harmonics.

D. 3D Reconstructed Electric Field Waveforms

We can further analyze the CP harmonics by considering their individual polarization states. Figure 4 a) shows the polarization states of the harmonics, which are produced as counter-rotating doublets. Figure 4 b) shows the 3D electric field temporal waveform $E = E_x + E_y$ of the incident counter-rotating fields. The total field (blue) traces out a trefoil-like pattern that rotates as a function of time. We observe a train of rotating attosecond pulses after applying a spectral filter between $10\omega_1$ and $20\omega_1$, as shown in Figure 4 c). The generated harmonics are counter-rotating, and therefore produce a complicated field structure that rotates as a function of time. The harmonics within this frequency range reach a peak amplitude of $a_0 = 2.1$ with an assumed central frequency of $\omega = 15\omega_1$.

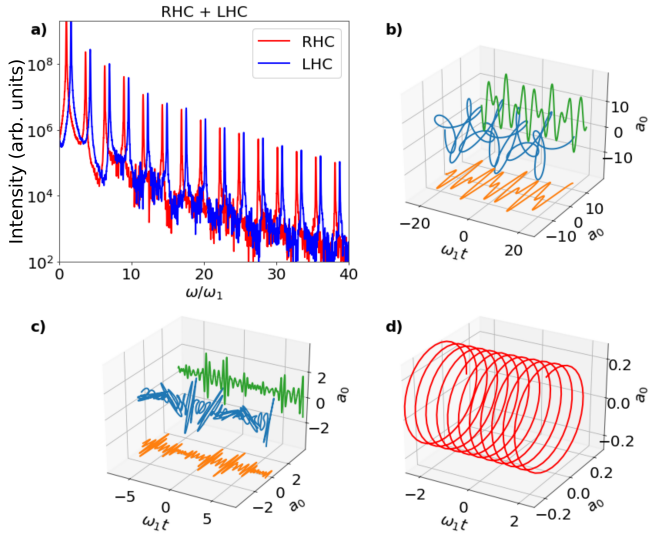

FIG. 4. Reconstructed 3D electric field waveforms of harmonics produced by counter-rotating fields with $\omega_2/\omega_1 = 1.65$ and $a_{0,1}/a_0 = 0.62$. 4 a) Reflected harmonic spectrum composed of counter-rotating doublets. 4 b) Waveform of the incident counter-rotating fields (blue) with orthogonal E_x (orange) and E_y (green) components. 4 c) Waveform of the harmonic pulse train (blue) after spectral filtering between $10\omega_1$ and $20\omega_1$ with orthogonal E_x (orange) and E_y (green) components. 4 d) Waveform of the $6\omega_1 + 5\omega_2$ harmonic.

Reducing the band-pass spectral filter width to isolate a single harmonic enables us to determine the harmonic eccentricity. The field eccentricity can be measured through the polarization ellipticity $\varepsilon = \min(E_x, E_y)/\max(E_x, E_y)$ and phase delay $\Delta\phi$. An LP field has no phase delay $\Delta\phi = 0$ between the fields, and a CP field has an $\varepsilon = 1$ and $\Delta\phi = \pm\pi/2$. When $\Delta\phi = \pi/2$ the field is right-circularly polarized, and when $\Delta\phi = -\pi/2$ the field is left-circularly polarized. A spectral filter of width $0.5\omega_1$ between $14\omega_1$ and $14.5\omega_1$ is applied to isolate the $6\omega_1 + 5\omega_2$ harmonic. The ellipticity and phase delay at the optimized ratio of $a_{0,1}/a_0 = 0.62$ are $\varepsilon = 0.89$ and $\Delta\phi = 0.51\pi$, respectively. Figure 4 d) shows a field map of the $6\omega_1 + 5\omega_2$ harmonic at $a_{0,1}/a_0 = 0.62$ showing the high degree of circularity in the electric field.

E. Optimization of Circularly-Polarized Harmonics

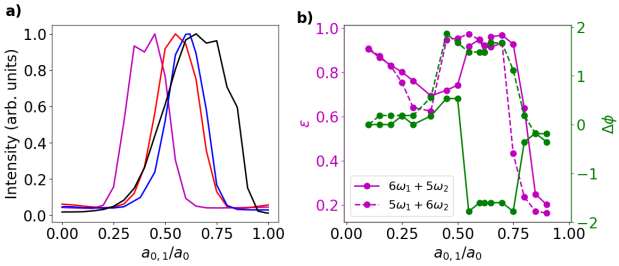

FIG. 5. Optimization of CP harmonics of counter-rotating fields. 5 a) Integrated intensity of $\omega_2/\omega_1 = 0.65$ (magenta), 1.35 (red), 1.65 (blue), and 2.5 (black) obtained by applying a spectral filter between $10 \leq \omega/\omega_1 \leq 40$. 5 b) Ellipticity and phase of harmonics $6\omega_1 + 5\omega_2$ (spectral filter between $14 \leq \omega/\omega_1 \leq 14.5$) and $5\omega_1 + 6\omega_2$ (spectral filter between $14.65 \leq \omega/\omega_1 \leq 15.15$) with varying $a_{0,1}/a_0$ for the case of $\omega_2/\omega_1 = 1.65$. The harmonics exhibit nearly-perfectly circular polarization near the optimal condition of $a_{0,1}/a_0 = 0.62$.

The optimization of CP harmonics depends strongly on the ratio of two-color field strengths. Figure 5 a) shows the integrated intensity of the generated harmonics for various frequency ratios $\omega_2/\omega_1 = 0.65$ (magenta), 1.35 (red), 1.65 (blue), and 2.5 (black) as a function of $a_{0,1}/a_0$ after applying a bandpass spectral filter between $10 \leq \omega/\omega_1 \leq 40$. The peak of the harmonic emission in this spectral range shifts according to the two-color frequency ratio. For example, for the case of $\omega_2/\omega_1 = 1.65$ the optimization occurs at occurs at $a_{0,1}//a_0 = 0.62$, or when the field intensities are equal. This optimization of the CP harmonics is narrow, the integrated intensity full width at half maximum is approximately equal to $a_{0,1}/a_0 \approx 0.22$ for the case of $\omega_2/\omega_1 = 1.65$, which requires careful control of the incident field intensities. Changes in the frequency ratio causes a shift in the optimal value of $a_{0,1}//a_0$, with individual optima occurring near the points of equal intensities for the two fields. The actual harmonic efficiency depends on many parameters like scale length and plasma density that were not adjusted.

For this case of $\omega_2/\omega_1 = 1.65$. Figure 5 b) shows an analysis of the polarization states of the harmonics $6\omega_1 + 5\omega_2 = 14.25\omega_1$ and $5\omega_1 + 6\omega_2 = 14.9\omega_1$ as functions of $a_{0,1}/a_0$. Spectral filters of widths $0.5\omega_1$ between $14 \leq \omega/\omega_1 \leq 14.5$ and $14.65 \leq \omega/\omega_1 \leq 15.15$ are applied to isolate the $6\omega_1 + 5\omega_2$ and $5\omega_1 + 6\omega_2$ harmonics, respectively. As stated previously, the ellipticity of the $6\omega_1 + 5\omega_2$ harmonic at the optimized ratio of $a_{0,1}/a_0 = 0.62$ is $\varepsilon(a_{0,1}/a_0 = 0.62) = 0.89$. However, the ellipticity of the harmonic on either side of this

optimization point is $\varepsilon(a_{0,1}/a_0 = 0.6) = 0.95$ and $\varepsilon(a_{0,1}/a_0 = 0.65) = 0.96$. Similarly, the phase delay between the field components for all three cases is $\Delta\phi = 0.51\pi$. Moving away from the optimal ratio of $a_{0,1}/a_0$ the polarization states become linearly-polarized as $\Delta\phi$ quickly approaches 0 as the harmonic intensity decreases.

F. Relativistic Critical Surface Motion

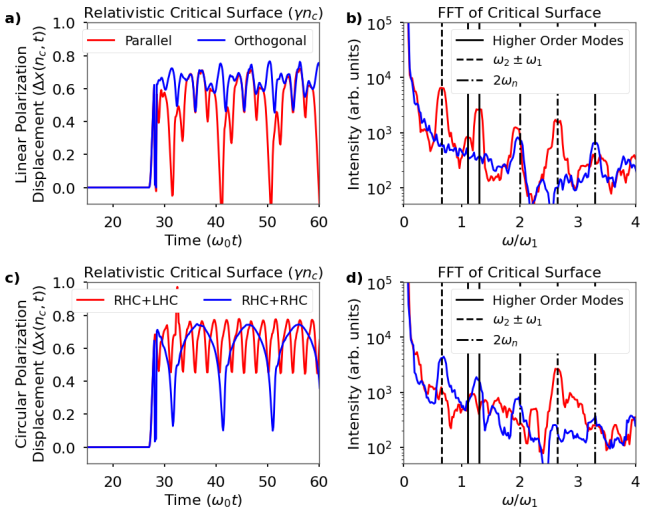

FIG. 6. Relativistic critical surface motion. 6 a) Parallel (red) and orthogoal (blue) LP fields drive the electron surface with different magnitudes and frequencies. 6 b) The oscillations from LP fields are dominated by beat frequencies, $\omega_2 \pm \omega_1$, in the parallel case, and $2\omega_2$ and $2\omega_1$, in the orthogonal case. 6 c) CP counter-rotating (red) and co-rotating (blue) fields produce oscillations in contrast with a single color interaction. 6 d) The CP fields produce oscillations dominated by the beat frequencies.

The displacement of the plasma relativistic critical surface $\Delta x(\gamma n_c, t)$ for the different polarization cases presented above is plotted in Figure 6. Figure 6 a) shows the position of the electron critical surface during the reflection of two-color laser fields with parallel (red) and orthogonal (blue) polarizations. Electron oscillations in the parallel polarization case are much stronger compared to the orthogonal polarization. Figure 6 b) Fourier transform of the LP-driven surface oscillations. The parallel polarization is dominated by beat frequency oscillations of the two fields $\omega_2 \pm \omega_1$, and twice the fundamental frequencies, $2\omega_1$ and $2\omega_2$; the orthogonal polarization contains only the modes from twice the fundamental frequencies. Figure 6 c) shows the oscillation of the critical surface for the two-color co-rotating and counter-rotating CP cases. Figure 6 d) shows that the critical surface oscillations of counter-rotating and co-rotating fields are dominated by the sum frequency, $\omega_2 + \omega_1$, and difference frequency, $\omega_2 - \omega_1$, of the fields, respectively.

IV. DISCUSSION

A. Harmonic Selection Rules

The harmonic frequencies generated during the reflection can be determined by the oscillation frequencies of the electron critical surface [6]. As the plasma critical surface oscillates along the laser axis, electrons located at the critical density surface are driven to relativistic velocities within an optical cycle. The resulting driving force from the laser coupled with the plasma pressure from the ions leads to a nonlinear, oscillating reflection surface of the plasma which changes as a function of time [34]. Therefore, a nonlinear phase shift, $\phi(t)$, is imparted by the oscillating mirror onto the laser field. This phase shift is determined by the oscillation modes, ω_m, of the mirror surface:

$$\phi(t) = \sum \phi_0 \sin(\omega_m t). \tag{5}$$

The reflected electric field, E_r, of the laser field is then given by

$$\begin{aligned} E_r &\propto \exp(-i\omega t)\exp i\phi(t) \\ &= \exp(-i\omega t)\sum_{n=-\infty}^{n=\infty} J_n \exp(-in\omega_m t), \end{aligned} \tag{6}$$

where J_n are Bessel functions of the first kind [6]. When the driving laser is a multi-cycle pulse the oscillation modes of the plasma surface are at frequencies linked to the laser optical cycle, and the re-radiated field in the spectral domain contains the higher order harmonics of the incident laser. At normal incidence, the only force capable of driving the mirror oscillations is the $v \times B$ component of the Lorentz force at frequency 2ω producing the odd harmonics $\omega_n = (2n+1)\omega$.

The two-color produce more complex surface oscillations leading to emission which contains multiple harmonic channels that are separate from the odd harmonics produced from a single frequency at either ω_1 or ω_2. A two-color laser pulse can be represented as a superposition of two single-color laser pulses defined by amplitudes $a_{0,1}$ and $a_{0,2}$ and central frequencies ω_1 and ω_2. An electromagnetic field with arbitrary polarization propagating in the $\hat{z}$-direction can be written in terms of the vector potential:

$$\mathbf{A}_i = \delta_i a_{0,i} \cos\omega_i t\ \hat{x} + (1-\delta_i^2)^{1/2} a_{0,i} \sin\omega_i t\ \hat{y}, \tag{7}$$

where δ_i is a polarization parameter defined such that $\delta_i = \pm 1, 0$ for an LP laser and $\pm 1/\sqrt{2}$ for a CP laser. The total vector potential of a general two-color laser field is then simply the summation of the two fields

$$\begin{aligned} \mathbf{A} = &[\delta_1 a_{0,1}\cos\omega_1 t + \delta_2 a_{0,2}\cos\omega_2 t]\hat{x} \\ &+[(1-\delta_1^2)^{1/2} a_{0,1}\sin\omega_1 t + (1-\delta_2^2)^{1/2} a_{0,2}\sin\omega_2 t]\hat{y}. \end{aligned} \tag{8}$$

For LP fields with parallel polarizations along the $\hat{x}$-direction, the total vector potential corresponds to the case of $\delta_1 = \delta_2 = 1$

$$\mathbf{A} = [a_{0,1}\cos\omega_1 t + a_{0,2}\cos\omega_2 t]\hat{x}. \tag{9}$$

For an electron initially at rest in a normal incidence geometry, the canonical momentum in the transverse direction is a conserved quantity, $\mathbf{p}_\perp = \mathbf{A}$, where $\mathbf{p}_\perp$ and $\mathbf{A}$ are the transverse electron momentum and laser vector potential, respectively. The longitudinal momentum, p_z, of the electron can be shown [37] to equal $p_z = (1-\mathbf{p}_\perp^2)/2$.

According to the theory of relativistic harmonic generation described by Baeva, *et al.* [34], the harmonic emission occurs when the magnitude of the transverse momentum of the critical surface electrons $\mathbf{p}_\perp$ reaches a minimum or vanishes. The transverse electron momenta is $p_x = a_{0,1}\cos\omega_1 t + a_{0,2}\cos\omega_2 t$ with amplitude,

$$\begin{aligned}|p_x| = (&a_{0,1}^2\cos^2\omega_1 t + a_{0,2}^2\cos^2\omega_2 t + \\ &2a_{0,1}a_{0,2}\cos(\omega_2+\omega_1)t + \\ &2a_{0,1}a_{0,2}\cos(\omega_2-\omega_1)t)^{1/2}.\end{aligned} \tag{10}$$

The electron surface oscillations contain four individual frequencies which are twice the fundamental frequencies $2\omega_1$ and $2\omega_2$ and the beat frequencies of $\omega_2 \pm \omega_1$, which are also seen in critical surface motion of Figure 6 b). The reflected field will therefore contain harmonic frequencies of the form $\Omega = \omega_{1,2} + 2n_1\omega_1 + 2n_2\omega_2 + n_3(\omega_1+\omega_2) + n_4(\omega_1-\omega_2)$ in agreement with the theoretical model of [14]. The generated harmonic frequencies can be rewritten in the form:

$$\Omega = (2n_1 + n_3 + n_4 + 1)\omega_1 + (2n_2 + n_3 - n_4)\omega_2 \tag{11}$$

$$\Omega = (2n_1 + n_3 + n_4)\omega_1 + (2n_2 + n_3 - n_4 + 1)\omega_2. \tag{12}$$

The individual terms of Equations 11 and 12 always have opposite parity, and it is possible to recast these selection rules for the parallel field polarization in the same form as Equation 1. For orthogonal fields, the electron surface oscillations are dominated by twice the fundamental frequencies of the incident fields, $2\omega_1$ and $2\omega_2$. The reflected field in this case yields harmonic frequencies of the form:

$$\Omega = (2n_1+1)\omega_1 + 2n_2\omega_2 \tag{13}$$

$$\Omega = 2n_1\omega_1 + (2n_2+1)\omega_2, \tag{14}$$

which similarly can be written in the form of Equation 1.

The general form of Equation 1 suggests that the ROM harmonic generation process is consistent with the quantum mechanical description of harmonic generation processes, wherein individual photons are summed together to generate one higher order photon. A restriction imposed by the symmetry of the normal-incidence interactions is that the oscillations modes limit the generated harmonics to those composed of an odd number of photons. These selection rules also indicate why the parallel polarization produces brighter harmonics for similar field strengths. Equations 11 and 12 contains two additional channels, n_3 and n_4, due to the presence of beat frequency oscillations that are lacking in the orthogonal HHG case, which increases the likelihood of their generation and the apparent brightness when compared to orthogonally-polarized fields.

Two-color, CP fields are capable of driving electron surface oscillations due to having minima in the transverse electric field [34]. For example, in the case of counter-rotating fields the field vector traces out a trefoil-type pattern when the intensities are equal whose number of lobes depend upon the frequency ratio, and contains a zero in the transverse electric field [20, 21, 38, 39]. Two circularly-polarized fields with opposite helicities corresponds to Equation 8 with $\delta_1 = 1/\sqrt{2}$ and $\delta_2 = -1/\sqrt{2}$

$$\begin{aligned}\mathbf{A} = &[\frac{a_{0,1}}{\sqrt{2}}\cos\omega_1 t - \frac{a_{0,2}}{\sqrt{2}}\cos\omega_2 t]\hat{x} \\ &+[\frac{a_{0,1}}{\sqrt{2}}\sin\omega_1 t + \frac{a_{0,2}}{\sqrt{2}}\sin\omega_2 t]\hat{y}.\end{aligned} \tag{15}$$

The transverse electron momenta is then given by

$$p_x = \tfrac{a_{0,1}}{\sqrt{2}}\cos\omega_1 t - \tfrac{a_{0,2}}{\sqrt{2}}\cos\omega_2 t \tag{16}$$

$$p_y = \tfrac{a_{0,1}}{\sqrt{2}}\sin\omega_1 t + \tfrac{a_{0,2}}{\sqrt{2}}\sin\omega_2 t, \tag{17}$$

and the amplitude of the transverse momenta is given by

$$|p_\perp| = \sqrt{a_{0,1}^2 + a_{0,2}^2 - 2a_{0,1}a_{0,2}\cos(\omega_2+\omega_1)t}. \tag{18}$$

The resulting mirror motion contains the single oscillation frequency at $\omega_2+\omega_1$, also seen in Figure 6 d). Therefore, the generated harmonics orders of the form $\Omega_+ = n\omega_2 + (n-1)\omega_1$ and $\Omega_- = (n-1)\omega_2 + n\omega_1$ are expected, which is consistent with the selection rules from Equations 2 and 3.

The observation of co-rotating harmonics from these simulations indicates that the co-rotating fields are driving electron oscillations at normal incidence. The field map of co-rotating fields contains one lob in the field structure, and an associated zero point [38]. The amplitude of the transverse electron motion in this case is given by

$$|p_\perp| = \sqrt{a_{0,1}^2 + a_{0,2}^2 + 2a_{0,1}a_{0,2}\cos(\omega_2-\omega_1)t}. \tag{19}$$

The co-rotating fields produce electron surface oscillations at frequency $\omega_2-\omega_1$, which generates harmonic orders of the form $\Omega = \omega_1 + n(\omega_2-\omega_1) = n\omega_2 - (n-1)\omega_1$, in agreement with Equation 4. While other schemes have shown circularly-polarized harmonics can be produced from elliptically-polarized laser fields [19], these schemes require oblique angles of incidence in order to drive electron surface oscillations.

Furthermore, for interactions with intensity profiles much longer than the carrier wavelength, carrier envelope phase (CEP) stabilization is not a requirement for efficient CP harmonic generation from normal incidence interactions as it would be in two-beam LP interactions. For two-color CP interactions varying the CEP is analogous to introducing a phase delay, which simply rotates the field structure of two-color CP pulses (see Supplemental Figure **??**). However, for few-cycle pulses with Gaussian or other temporally-varying profiles, a change in CEP would change the locations of the electric field extrema and therefore impact the efficiency of the HHG process.

Incidentally, the presence of harmonic doublets in the counter-rotating case is consistent with the quantum model of the conservation of spin-angular momentum, where the final photon generated from the interaction must have photon spin

TABLE I. Normal incidence harmonic selection rules for linear and circularly polarized two-color fields.

Field Types	ω_1 Pol.	ω_2 Pol.	Selection Rules	Harmonic Polarization
LP	E_x	E_x	$\Omega = n_1\omega_1 + n_2\omega_2$	E_x
LP	E_x	E_y	$\Omega = n_1\omega_1 + n_2\omega_2$	45° between E_x and E_y
CP	RHC	LHC	$\Omega_{+,-} = n\omega_{2,1} + (n-1)\omega_{1,2}$	LHC, RHC
CP	RHC	RHC	$\Omega = n\omega_2 - (n-1)\omega_1$	RHC

$\sigma = \pm 1$. In this model, the counter-rotating harmonic doublets are being generated from the linear addition of photons from each field such that each harmonic in the doublet has one extra photon from either field in order to preserve $\sigma = \pm 1$. The presence of a single harmonic channel for the co-rotating fields as opposed to two harmonic channels for the counter-rotating case is also consistent with the spin-angular momentum conservation, where the final harmonic must be generated with the same spin as the incident fields. Furthermore, due to the inherent phase matching of ROM, the co-rotating fields can produce harmonics while in the tunnel ionization regime they are forbidden.

The normal incidence selection rules for two-color, LP and CP fields are summarized in Table I. The harmonic polarization of linearly-polarized, parallel fields are along the same polarization axis as the fundamental fields. Orthogonally-polarized fields with one color polarized along E_x and the other polarized along E_y produced harmonics with polarization at 45° between the incidence fields. Counter-rotating, CP fields produce harmonic doublets with counter-rotating polarization and co-rotating, CP fields produce rapidly decaying harmonics that are the same helicity as the incident fields.

B. Optimization of Two-Color Harmonic Generation

As discussed in Section III E there is an optimization of harmonic emission in terms of $a_{0,1}/a_0$ that changes as a function frequency ratio ω_2/ω_1. This can be understood for the CP cases by considering how the total electric field strength varies for a two-color field. The electric field of two-color, CP fields can be calculated by $\mathbf{E} = -\partial\mathbf{A}/\partial t$. The magnitude of the electric field is given by

$$|E| = \frac{1}{\sqrt{2}}\sqrt{a_{0,1}^2\omega_1^2 + a_{0,2}^2\omega_2^2 + 2a_{0,1}a_{0,2}\omega_1\omega_2\cos(\omega_2 \pm \omega_1)t}, \tag{20}$$

where oscillatory frequency sign corresponds to $+$ for counter-rotating fields, and $-$ for co-rotating fields.

The optimal conditions for harmonic generation are when the transverse electron momentum vanishes, i.e. when the transverse electric field goes to zero according to Baeva, et al. [34]. The optimization condition for the two-color counter-rotating fields can be found by determining when the minimum of Equation 20 equals zero,

$$a_{0,1}\omega_1 = a_{0,2}\omega_2. \tag{21}$$

Written in terms of laser intensity, the minimization occurs when the two fields are of equal intensity $I_1 = I_2$, regardless of frequency ratio and for both counter-rotating and co-rotating fields.

This optimization point for CP harmonic generation can be understood through an analogous quantum mechanical picture of conservation of spin-angular momentum in the circularly-polarized case, which need on average an equal number of photons from each field, i.e. equal field intensities, for circularly-polarized harmonics to be generated efficiently.

C. Robustness of Two-Beam Harmonic Generation

The presented results were all from a select few parameters of laser and plasma conditions that can be experimentally achieved by current laser systems. In addition, parameter scans were conducted to determine the effects of phase delay between $0 < \Delta\phi < 2\pi$, temporal delay between $0 < t/T_1 < 1$, ratio of the normalized vector potentials between $0 < a_{0,1}/(a_{0,1} + a_{0,2}) < 1$, total vector potential $0.1 < a_0 = a_{0,1} + a_{0,2} < 100$, laser pulse duration, laser pulse profile, pre-plasma scale length $0.002 < L_s/\lambda_1 < 1$, and bulk plasma density between $1 < n_e/n_c < 1000$. We found that general trends of these parameter scans were consistent with the presented results. As described in sections III C, III E, and IV B the generated harmonic frequencies and their optimization point depend upon the input frequency ratio of the two-beams. Furthermore, we found that the two-color HHG mechanism and derived selection rules are robust to changes in pulse shape, intensity, pre-plasma scale length (see Supplemental Material).

V. CONCLUSION

In this paper, we have studied the interaction of relativistically-intense, two-color laser fields with overdense plasmas. By combining non-commensurate fields with frequencies ω_1 and ω_2, we have shown that the relativistic harmonic generation process is a robust mechanism to control the polarization and frequency of emitted photons by tuning the incident field properties such as polarization and frequency ratio. The benefit of driving two-color harmonic generation enables the possibility of generating frequency-tunable harmonics with controllable polarization states. We have found that the two-color harmonic generation optimization occurs for a similar intensity ratio of the two driving fields, regardless of the incident polarization states.

While not discussed in this work, there are interesting phenomena that are exclusive to multi-dimensional effects, e.g. oblique angles of incidence that are already being explored

from single-color interactions that may have significant effects from two-color interactions. For example, the interaction of a elliptically-polarized laser at an oblique incidence has been shown to produce circularly-polarized harmonics with high efficiency[19]. The influence of spectral phase, which has already been shown to produce isolated attosecond pulses from gas target harmonic generation [40, 41], may impact spatial and temporal varying frequency generation in the relativistic regime [42].

Future, two-color experiments can be designed to exploit optimizations discussed in this work. Experiments which have polarization and intensity control of their incident fields can optimize harmonic generation through varying the individual field intensities during linearly-polarized interactions, before rotating their individual polarizations to produce circularly-polarized harmonics.

Advancing table-top laser technology has enabled high repetition rate systems with smaller beam diameters to produce intensities sufficient to study these relativistic interactions. Combined with higher stability system, wavelength-tunable relativistic harmonic generation experiments are now possible through the manipulation of the fundamental laser wavelength through nonlinear optical processes such as frequency-doubling [43] and OPA [44, 45]. High-power OPA systems such as the L1 Allegra at ELI Beamlines and the proposed EP OPAL system at the Laboratory for Laser Energetics [25] are ideal systems to perform two-color, relativistic harmonic generation through tunable, non-commensurate wavelengths.

ACKNOWLEDGMENTS

This work was supported by the National Science Foundation (CAREER: National Science Foundation under Grant No. PHY-1753165; STROBE: A National Science Foundation Science & Technology Center under Grant No. DMR-1548924). We acknowledge the OSIRIS consortium (UCLA/IST Portugal) for providing access to the OSIRIS 4.0 Framework (work supported by NSF ACI-1339893). Simulations were performed on the Green Planet cluster at the University of California, Irvine (supported by NSF Grant CHE-0840513).

Appendix: Supplemental Information

1. Pulse Profile Comparison

The flattop temporal profile used in these simulations is an idealized version of the temporal profile of a laser pulse, and does not represent the real temporal profile of high-power laser systems, particularly those with pulse durations on the order of tens of femtoseconds. To ensure that the physics discussed in this study is applicable both in this idealized case and with real Gaussian laser pulses we have performed comparison, two-beam simulations of both flattop and Gaussian temporal profiles as presented in Figure 7. The selected frequency ratio was $\omega_2/\omega_1 = 1.65$ and the total normalized vector potential was $a_0 = 10$. Two polarization states are presented, linearly-polarized (LP) with parallel polarization and counter-rotating circularly-polarized (CP). The incident electric fields for the LP and CP cases are shown in Figures 7 a) and 7 b) for the flattop (red) and Gaussian (blue) pulse profiles. The reflected harmonic spectra are shown in Figures 7 c) and 7 d) for the LP and CP cases, respectively. The harmonic spectra in both the LP and CP cases contain the same harmonic orders regardless of pulse shape. The consistent harmonic orders observed allows us to simplify the analysis of the critical surface motion and provides a better representation of the data to the reader.

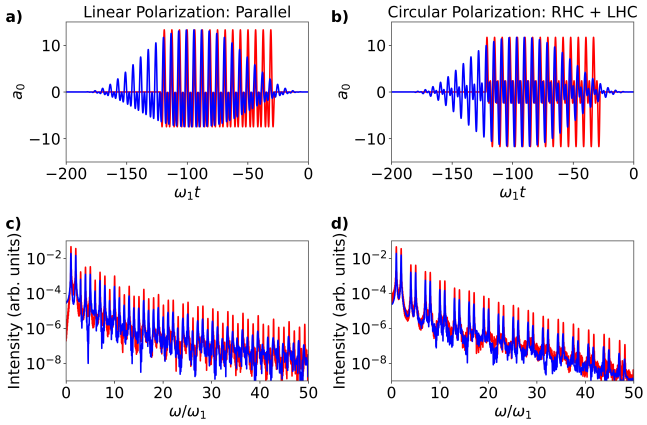

FIG. 7. Comparison of two-beam HHG driven by flattop (red) and Gaussian (blue) pulse profiles. Incident fields, 7 a), and reflected harmonic spectra, 7 c), for linearly-polarized fields with parallel polarization. Incident fields, 7 b), and reflected harmonic spectra, 7 d), for circularly-polarized fields with counter-rotating polarization.

2. Pulse Duration Comparison

As a laser pulse shortens in time, and approaches the few cycle limit, the generated harmonics from high harmonic generation interactions necessarily broaden in the frequency domain. The choice to use a relatively long pulse length of nine optical cycles was to easily discriminate between the individual harmonic orders produced during the interaction. To highlight this point, we investigated the few-cycle regime of the interaction between two-color laser pulses with frequency ratio $\omega_2/\omega_1 = 1.3$ with counter-rotating circular polarizations. These simulations were performed using a Gaussian pulse shape of varying full-width at half-maximum of 1.9, 3.7, and 11.2 optical cycles (5 fs, 10 fs, and 30 fs for an 800 nm laser). For these interactions, the normalized vector potential was not varied to account for a difference in pulse duration, and therefore the total energy of the interactions are not constant. The resulting CP harmonics can be seen in the plot below. For the long pulse duration case (11.2 cycles) a counter-rotating harmonic doublet can be clearly resolved. However, as the laser pulse duration shortens, this doublet merges into what appears as a single broader harmonic.

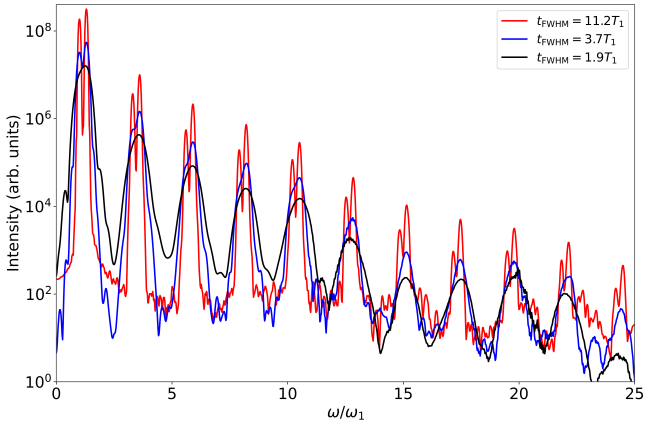

FIG. 8. Comparison of two-beam HHG driven by different full-width at half-maximum pulse durations of 11.2 (red), 3.7 (blue), and 11.2 (black) optical cycles.

3. Carrier Envelope Phase and Temporal Delay

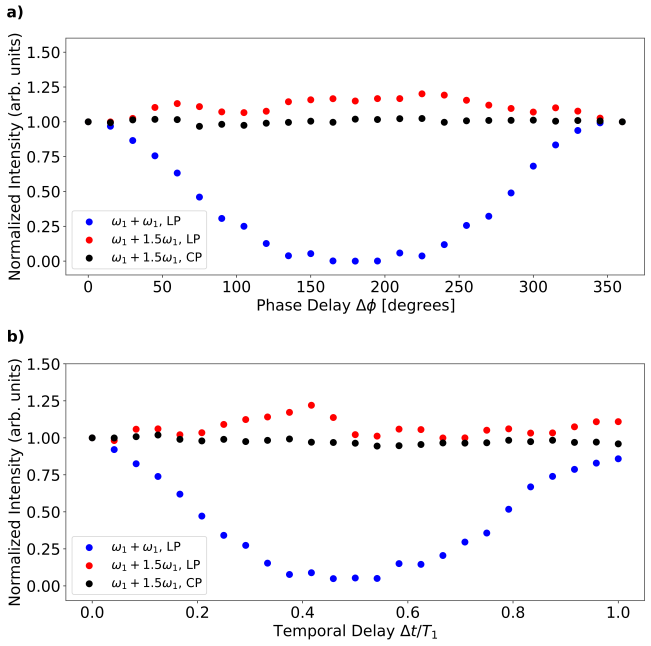

FIG. 9. Integrated harmonic intensity of two-beam interactions with varying carrier envelope phase delay.

We investigated the role of a shift in the CEP and temporal delay between the two color pulses during the interaction. The simulations were initialized with the same conditions as discussed in the Methods, but with a variable CEP or temporal delay of one of the pulses. We investigated three cases: two LP fields with the same frequency, ω_1, which was used as a reference, two LP fields with frequency ratio $\omega_2/\omega_1 = 1.5$, and two CP fields with frequency ratio $\omega_2/\omega_1 = 1.5$. For all three cases the two field intensities were set to be equal. The integrated harmonic intensity between $10 \leq \omega/\omega_1 \leq 40$ were then normalized to the intensity of the zero delay cases.

Figure 9(a) shows the impact of CEP on the harmonic efficiency, and is most apparent in the single frequency case, where a phase delay of 180° leads to a perfect destructive interference and no harmonic emission. The LP two-color case produces a small enhancement (< 20%) of the integrated harmonic intensity. The CP two-color case does not significantly change the efficiency of the harmonic emission, which is consistent with the discussion above. Therefore, in experiments that have CEP control, introducing slight shifts in the CEP of one with respect to the other may lead to an enhancement of the harmonic emission.

Figure 9(b) shows impact of the time delay on the harmonic efficiency, and again is most apparent in the single frequency case, where a phase delay of half an optical cycle leads to almost perfect destructive interference and very little harmonic emission. The linearly-polarized two-color case produces a small enhancement ($\sim$ 20%) of the integrated harmonic intensity, which is similar to the CEP case above. The circularly-polarized two-color case does not significantly change the efficiency of the harmonic emission. Therefore, in experiments that have temporal control on the order of the optical period, introducing slight shifts of one with respect to the other may lead to an enhancement of the harmonic emission.

4. Normalized Vector Potential

Figure 10 shows that two-color HHG occurs occurs for a_0 values of 1, 10, and 100 with varying efficiencies for the frequency ratio of $\omega_2/\omega_1 = 1.65$. In both parallel LP 10 a) and counter-rotating CP 10 b) the efficiency of the interaction increases with a_0. The results presented in the main body are at a total normalized vector potential $a_0 = 10$. This intensity was chosen as it can consistently be achieved in many current or upcoming petawatt-class facilities worldwide. In order to drive relativistic harmonic generations, the vector potential requirement of the lasers needs to be $a_0 \gtrsim 1$, which is well-known from single-beam studies.

5. Pre-plasma Scale Length

Figure 11 shows the impact of pre-plasma scale length on the generation of two-color harmonics. The presented harmonics are from the interaction of two-beams with frequency ratio $\omega_2/\omega_1 = 1.65$ and $a_0 = 10$, and are circularly-polarized in counter-rotating directions. The efficiency of harmonic generation in this case strongly depends upon the pre-plasma scale length, which has an optimal value near $L_s = 0.318\lambda_1$.

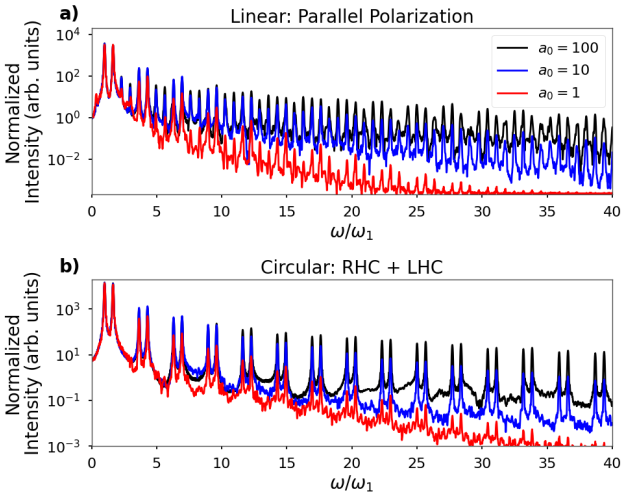

FIG. 10. Reflected harmonic spectra for frequency ratio $\omega_2/\omega_1 = 1.65$ and $a_0 = 1$ (red), 10 (blue), and 100 (black). 10 a) Linearly-polarized, parellel fields. 10 b) Circularly-polarized, counter-rotating fields.

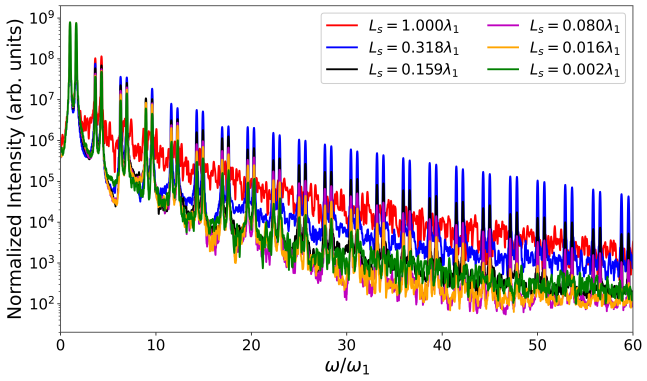

FIG. 11. Reflected harmonic spectra from two-beams with frequency ratio $\omega_2/\omega_1 = 1.65$ and $a_0 = 10$ for various pre-plasma scale lengths L_s.

[1] S. Gordienko, A. Pukhov, O. Shorokhov, and T. Baeva, Phys. Rev. Lett. **93**, 115002 (2004).
[2] N. M. Naumova, J. A. Nees, and G. A. Mourou, Physics of Plasmas **12**, 056707 (2005).
[3] B. Dromey, M. Zepf, A. Gopal, K. Lancaster, M. S. Wei, K. Krushelnick, M. Tatarakis, N. Vakakis, S. Moustaizis, and R. Kodama, Nat. Phys. **2**, 456 (2006).
[4] U. Teubner and P. Gibbon, Rev. Mod. Phys. **81**, 445 (2009).
[5] S. V. Bulanov, N. M. Naumova, and F. Pegoraro, Physics of Plasmas **1**, 745 (1994).
[6] D. Von der Linde and K. Rzazewski, Appl. Phys. B **63**, 499 (1996).
[7] R. Lichters, J. Meyer-ter-Vehn, and A. Pukhov, Phys. Plasmas **3**, 3425 (1996).
[8] P. Gibbon, Phys. Rev. Lett. **76**, 50 (1996).
[9] D. an der Brügge and A. Pukhov, Physics of Plasmas **17**, 033110 (2010).
[10] J. M. Mikhailova, M. V. Fedorov, N. Karpowicz, P. Gibbon, V. T. Platonenko, A. M. Zheltikov, and F. Krausz, Phys. Rev. Lett. **109**, 245005 (2012).
[11] B. Dromey, S. Rykovanov, M. Yeung, R. Hörlein, D. Jung, D. C. Gautier, T. Dzelzainis, D. Kiefer, S. Palaniyppan, and R. Shah, Nat. Phys. **8**, 804 (2012).
[12] A. A. Gonoskov, A. V. Korzhimanov, A. V. Kim, M. Marklund, and A. M. Sergeev, Phys. Rev. E **84**, 046403 (2011).
[13] T. G. Blackburn, A. A. Gonoskov, and M. Marklund, Phys. Rev. A **98**, 023421 (2018).
[14] S. Mirzanejad and M. Salehi, Phys. Rev. A **87**, 063815 (2013).
[15] M. R. Edwards, V. T. Platonenko, and J. M. Mikhailova, Opt. Lett., OL **39**, 6823 (2014).
[16] M. R. Edwards and J. M. Mikhailova, Phys. Rev. Lett. **117**, 125001 (2016).
[17] M. R. Edwards and J. M. Mikhailova, Phys. Rev. A **93**, 023836 (2016).
[18] M. Yeung, S. Rykovanov, J. Bierbach, L. Li, E. Eckner, S. Kuschel, A. Woldegeorgis, C. Rödel, A. Sävert, G. G. Paulus, M. Coughlan, B. Dromey, and M. Zepf, Nat. Photonics **11**, 32 (2017).
[19] Z.-Y. Chen and A. Pukhov, Nat. Commun. **7**, 12515 (2016).
[20] Z.-Y. Chen, Phys. Rev. E **97**, 043202 (2018).
[21] D. Xie, Y. Yin, T. Yu, H. Zhou, Z. Chen, and H. Zhuo, Plasma Sci. Technol. **23**, 045502 (2021).
[22] A. Fleischer, O. Kfir, T. Diskin, P. Sidorenko, and O. Cohen, Nat. Photonics **8**, 543 (2014).
[23] O. Kfir, P. Grychtol, E. Turgut, R. Knut, D. Zusin, D. Popmintchev, T. Popmintchev, H. Nembach, J. M. Shaw, A. Fleischer, H. Kapteyn, M. Murnane, and O. Cohen, Nat. Photonics **9**, 99 (2015).
[24] D. D. Hickstein, F. J. Dollar, P. Grychtol, J. L. Ellis, R. Knut, C. Hernández-García, D. Zusin, C. Gentry, J. M. Shaw, T. Fan, K. M. Dorney, A. Becker, A. Jaroń-Becker, H. C. Kapteyn, M. M. Murnane, and C. G. Durfee, Nat. Photonics **9**, 743 (2015).
[25] J. Bromage, S.-W. Bahk, I. A. Begishev, C. Dorrer, M. J. Guardalben, B. N. Hoffman, J. B. Oliver, R. G. Roides, E. M. Schiesser, M. J. S. Iii, M. Spilatro, B. Webb, D. Weiner, and J. D. Zuegel, High Power Laser Sci. Eng. **7**, 10.1017/hpl.2018.64 (2019/ed).
[26] J. Bromage, S.-W. Bahk, I. A. Begishev, S. Bucht, C. Dorrer, C. Feng, B. N. Hoffman, C. Jeon, C. Mileham, J. B. Oliver, R. G. Roides, M. J. Shoup, M. Spilatro, B. Webb, and J. D. Zuegel, in *Conf. Lasers Electro-Opt. 2021 Pap. STh4N1* (Optical Society of America, 2021) p. STh4N.1.
[27] R. A. Fonseca, L. O. Silva, F. S. Tsung, V. K. Decyk, W. Lu, C. Ren, W. B. Mori, S. Deng, S. Lee, T. Katsouleas, and J. C. Adam, in *Comput. Sci. — ICCS 2002*, edited by P. M. A. Sloot, A. G. Hoekstra, C. J. K. Tan, and J. J. Dongarra (Springer Berlin Heidelberg, 2002) pp. 342–351.
[28] P. Mora, Phys. Rev. Lett. **90**, 185002 (2003).
[29] M. Behmke, D. an der Brügge, C. Rödel, M. Cerchez, D. Hemmers, M. Heyer, O. Jäckel, M. Kübel, G. G. Paulus, G. Pretzler, A. Pukhov, M. Toncian, T. Toncian, and O. Willi, Phys. Rev.

Lett. **106**, 185002 (2011).
[30] C. Rödel, D. an der Brügge, J. Bierbach, M. Yeung, T. Hahn, B. Dromey, S. Herzer, S. Fuchs, A. G. Pour, E. Eckner, M. Behmke, M. Cerchez, O. Jäckel, D. Hemmers, T. Toncian, M. C. Kaluza, A. Belyanin, G. Pretzler, O. Willi, A. Pukhov, M. Zepf, and G. G. Paulus, Phys. Rev. Lett. **109**, 125002 (2012).
[31] F. Dollar, P. Cummings, V. Chvykov, L. Willingale, M. Vargas, V. Yanovsky, C. Zulick, A. Maksimchuk, A. G. R. Thomas, and K. Krushelnick, Phys. Rev. Lett. **110**, 175002 (2013).
[32] J. H. Easter, A. G. Mordovanakis, B. Hou, A. G. Thomas, J. A. Nees, G. Mourou, and K. Krushelnick, Opt. Lett. **35**, 3186 (2010).
[33] M. Zepf, G. D. Tsakiris, G. Pretzler, I. Watts, D. M. Chambers, P. A. Norreys, U. Andiel, A. E. Dangor, K. Eidmann, C. Gahn, A. Machacek, J. S. Wark, and K. Witte, Phys. Rev. E **58**, R5253 (1998).
[34] T. Baeva, S. Gordienko, and A. Pukhov, Phys. Rev. E **74**, 046404 (2006).
[35] M. R. Edwards and J. M. Mikhailova, Sci Rep **10**, 5154 (2020).
[36] Q. Li, X. Xu, X. Xu, Y. Wu, Y. Yin, D. Zou, T. Yu, and T. Yu, Opt. Express, OE **30**, 15470 (2022).
[37] P. Gibbon, *Short Pulse Laser Interactions with Matter* (Imperial College Press, London, 2005).
[38] C. A. Mancuso, D. D. Hickstein, P. Grychtol, R. Knut, O. Kfir, X.-M. Tong, F. Dollar, D. Zusin, M. Gopalakrishnan, C. Gentry, E. Turgut, J. L. Ellis, M.-C. Chen, A. Fleischer, O. Cohen, H. C. Kapteyn, and M. M. Murnane, Phys. Rev. A **91**, 031402 (2015).
[39] K. M. Dorney, J. L. Ellis, C. Hernández-García, D. D. Hickstein, C. A. Mancuso, N. Brooks, T. Fan, G. Fan, D. Zusin, C. Gentry, P. Grychtol, H. C. Kapteyn, and M. M. Murnane, Phys. Rev. Lett. **119**, 063201 (2017).
[40] C. Altucci, R. Esposito, V. Tosa, and R. Velotta, Opt. Lett., OL **33**, 2943 (2008).
[41] C. Altucci, R. Velotta, V. Tosa, P. Villoresi, F. Frassetto, L. Poletto, C. Vozzi, F. Calegari, M. Negro, S. D. Silvestri, and S. Stagira, Opt. Lett., OL **35**, 2798 (2010).
[42] E. Porat, I. Cohen, A. Levanon, and I. Pomerantz, Phys. Rev. Research **4**, L022036 (2022).
[43] A. Tarasevitch, K. Lobov, C. Wünsche, and D. von der Linde, Phys. Rev. Lett. **98**, 103902 (2007).
[44] A. V. Mitrofanov, D. A. Sidorov-Biryukov, M. V. Rozhko, S. V. Ryabchuk, A. A. Voronin, and A. M. Zheltikov, Opt. Lett., OL **43**, 5571 (2018).
[45] N. Beier, T. Nguyen, J. Lin, J. Nees, K. Krushelnick, and F. Dollar, New J. Phys. **21**, 043052 (2019).